Journal of Environmental Chemical Engineering 10 (2022) 107891

Contents lists available at ScienceDirect

Journal of Environmental Chemical Engineering

journal homepage: www.elsevier.com/locate/jece

Fe(III)-exchanged zeolites as efficient electrocatalysts for Fenton-like oxidation of dyes in aqueous phase

Zineb Bencheqroun [a,g], Nihat E. Sahin [d], Olívia S.G.P. Soares [d,e], Manuel F.R. Pereira [d,e], Hicham Zaitan [i], Mustapha Nawdali [h], Elisabetta Rombi [f], António M. Fonseca [a,b,c], Pier Parpot [a,b,c,*], Isabel C. Neves [a,b,c,*]

[a] CQUM - Centre of Chemistry, University of Minho, 4710-057, Portugal
[b] CEB - Centre of Biological Engineering, University of Minho, 4710-057 Braga, Portugal
[c] LABBELS – Associate Laboratory, Braga, Guimarães, Portugal
[d] LSRE-LCM - Laboratory of Separation and Reaction Engineering – Laboratory of Catalysis and Materials, Faculty of Engineering, University of Porto, Portugal
[e] ALiCE - Associate Laboratory in Chemical Engineering, Faculty of Engineering, University of Porto, Portugal
[f] Dipartimento di Scienze Chimiche e Geologiche, Università di Cagliari, Complesso Universitario di Monserrato, 09042 Monserrato, Italy
[g] Laboratoire de Chimie de la Matière Condensée, Faculté des Sciences et Techniques, Fès, Morocco
[h] Laboratoire de Chimie de la Matière Condensée, Faculté de Polydisciplinaire, Université Sidi Mohamed Ben Abdellah, Taza, Morocco
[i] Laboratory of Processes, Materials and Environment (LPME), Department of Chemistry, Faculty of Science and Technology of Fez, Sidi Mohamed Ben Abdellah University, B.P. 2202, Fez, Morocco

ARTICLE INFO

Editor: Xin Yang

Keywords:
Fe(III)-zeolite-modified electrodes
Fenton-like oxidation
Dyes/water
Room temperature
Without H_2O_2

ABSTRACT

Electrochemical oxidation, a powerful tool for the conversion of several of organic dye compounds using metal-exchanged zeolite modified electrodes, has shown great potential due to its capability of high efficiency degradation, a global priority for a sustainable environment. In this study, the role of the Fe(III)-exchanged-zeolite-modified electrodes using two different zeolite structures (such as FAU (Y) and MFI (ZSM-5)) on the Fenton-like oxidation of Congo Red dye ($C_{32}H_{22}N_6Na_2O_6S_2$) was investigated at room temperature. To clarify the electrocatalytic trend observed by constant potential electrolysis, the surface acidity of the catalysts prepared by ion-exchange method was determined by microcalorimetric measurements of ammonia adsorption. The different acid properties deriving from the presence of different cations (NH_4^+, H^+ and Na^+) in the case of MFI structure were found to enhance the ion-exchange capacity as well as the oxidation reaction. MFI catalysts - Fe(Na)ZSM-5, Fe(H)ZSM-5 and Fe(NH_4)ZSM-5 - exhibited excellent activity and stability at the end of the electrolysis (within 60 min), with a total dye degradation and an higher mineralization on Fe(H)ZSM-5 (64% of TOC), compared with Fe(Na)Y_{nano}, which takes twice as long (120 min) for total degradation, with 19% of TOC removal. This work provides an effective route for the development of stable Fe(III)-zeolite-modified electrodes for electro-Fenton oxidation, with a better stabilization of Fe^{3+} ions within the framework, without the aggregation of iron and the addition of H_2O_2, at room temperature.

1. Introduction

Zeolites are a family of porous materials based in alumino-silicates and possess a well-defined microporous (subnanometer to 2 nm) system and a crystalline framework, which play a key role in various industrial processes owing to their multi-functional transparency of the tuneable structure [1]. Their frameworks act as both host material and nanoreactor, allowing an effective environment for catalytic and electrocatalytic reactions. Especially, physicochemical properties of a guest material are most likely contributing to electrical conductivity, and thus improve the targeted reaction rate and selectivity [1–4]. The electrical conductivity in zeolites has been ascribed to the movement and the stabilization of the metal ions inside the structure, which confer high specific selectivity for different applications [1,5,6]. To date, numerous efforts have been devoted to the development of guest-host zeolite materials as adsorbents [7,8], heterogeneous catalysts and ion-exchangers [1–3]. In addition, due to their stability in biological environments, these structures found applications in biomedical fields

* Corresponding authors at: CQUM - Centre of Chemistry, University of Minho, 4710-057, Portugal.
E-mail addresses: parpot@quimica.uminho.pt (P. Parpot), ineves@quimica.uminho.pt (I.C. Neves).

https://doi.org/10.1016/j.jece.2022.107891
Received 1 March 2022; Received in revised form 6 May 2022; Accepted 8 May 2022
Available online 16 May 2022

[9,10]. However, the use of zeolites in electrocatalysis is few explored [11–14].

In recent years, water treatment technologies have been of economic importance due to purified drinking water demand depending on the rapidly increasing world population. Among the various technologies, the electrochemical degradation process is attractive and promising for wastewater treatment, being capable of degrading organic compounds including synthetic dyes. In this emerging process, organic matter is mineralized by mediated oxidation with reactive oxygen species, principally with the hydroxyl radical ($HO^{\bullet}$) generated *in situ* at the surface of the high-current anode [15]. The $HO^{\bullet}$ radical is the strongest oxidant after fluorine and its high standard redox potential ($E^{\circ} = 2.80$ V/SHE) permits the complete degradation of most organic matter into CO_2, inorganic ions, and water. This treatment technology has different advantages such as environmental compatibility, polyvalence, energy efficiency, and cost-effectiveness [16]. In addition, the most interesting advantage of this process is that it does not require the external addition of reagents for the production of hydroxyl radicals [17].

The modified electrodes have the capacity to provide low potentials and high peak current intensities, giving superior sensitivity and selectivity when compared to smooth support electrodes. However, the use of Fe-based electrodes has a major disadvantage related to the formation of iron-containing sludge, which requires catalyst recovery after treatment, making the process uneconomical [17]. This disadvantage can be overcome by developing heterogeneous catalysts, through the incorporation of Fe ions in porous supports. These ions are stabilized by the zeolite structure and generate $HO^{\bullet}$ without the precipitation of iron [14, 18–20]. Fe-exchanged zeolites act as catalysts for the heterogeneous Fenton reaction, where the reactions occur, as showed in [19], and the redox cycle between the different valence states of Fe (Fe^{3+}/Fe^{2+}) is enhanced by the presence of the host support. Recently, we reported that Fe^{3+} exchange in zeolite boosts the Fenton-like reaction, which confirms that ion species promote the redox cycle of the iron [14] as described in Eqs. (1) and (2):

$$Fe(III) - zeolite + H_2O_2 \rightarrow Fe(II) - zeolite + HO_2^{\bullet} + H^+ \quad (1)$$

$$Fe(II) - zeolite + H_2O_2 \rightarrow Fe(III) - zeolite + HO^{\bullet} + OH^- \quad (2)$$

Precious insights have been gained in the understanding of electrochemical degradation of dye compounds using different modified electrodes, and the development of appropriate electrode material is crucial to the degradation efficiency of industrial processes [20–23]. Within this perspective, iron-exchanged zeolites were prepared by using a facile and cost-effective ion-exchange method that introduces metal ions into the zeolite framework. Moreover, Fe-exchanged zeolites with excellent activity were reported using Congo Red dye, providing comprehensive evidence to the utilization of these modified electrode materials as anode oxidant in the electrodegradation process in electro Fenton-like oxidation. This perspective particularly enlightens the capacity of electrodegradation to maximize activity, selectivity, and durability in the removal of organic dye compounds, as well as to provide a rational pathway for the development and design of the metal-exchanged zeolites.

2. Experimental

2.1. Preparation of the Fe-exchanged zeolite samples

Preparation of Fe-exchanged zeolite samples using a simple and effective ion-exchange method with an improved process for directly introducing ferric ions in the zeolite structures is reported in the following. Two zeolite structures in powder form, MFI ((NH_4)ZSM-5, CBV 3024E from Zeolyst International) and FAU (NaY_{nano}, NanoFAU-Y from NanoScape, with nanoparticles of 150 nm) were used as pristine supports for preparing the samples. NaY_{nano} and (NH_4)ZSM-5 were dehydrated at 120 °C overnight before the successive preparation steps. HZSM-5 was prepared by calcination of (NH_4)ZSM-5 at 500 °C for 8 h under a dry air stream that allows decomposition of the ammonium ions of the structure, whereas (Na)ZSM-5 was prepared by the ammonium form through ion exchange of NH_4^+ with Na^+ using a $NaNO_3$ solution, as described in [24]. Furthermore, Fe-exchanged zeolite samples (herein labelled as Fe(Na)Y_{nano}, Fe(NH_4)ZSM-5, Fe(H)ZSM-5, and Fe(Na) ZSM-5) were prepared by a simple protocol in order to increase the density of catalytic sites and improve the electron transfer efficiency [14,18]. Briefly, 3.65 mmol of Fe^{3+} ions in aqueous solution, from the precursor iron(III) nitrate nonahydrate ($Fe(NO_3)_3.9\ H_2O$, 99.95% trace metal basis, purchased from Sigma-Aldrich) in ultra-pure water (18.2 MΩ cm at 20 °C) were added to an appropriate amount of different pristine zeolites at room temperature (iron(III) solution/zeolite weight ratio equal to 35) and the pH was adjusted to 4.0 in order to prevent the precipitation of iron. The suspension was then maintained under stirring (300 rpm) for 24 h in order to enhance the ion-exchange process; finally, it was filtered off and washed several times with ultra-pure water. The recovered solid was then dried in an oven at 80 °C for 24 h, followed by a calcination step at 350 °C with a temperature rate of 5 °C min^{-1} for 4 h in a static oven.

2.2. Physicochemical characterization of iron(III)-exchanged zeolites

X-ray diffraction (XRD) patterns of the samples were recorded by a D8 Advance diffractometer in Bragg-Brentano (θ-θ) configuration with CuKα radiation at the wavelength of 1.5406 Å, the voltage and tube current being 40 kV and 40 mA, respectively. The diffraction patterns were collected in a range of 2θ from 3° to 60° with a step size of 0.05° and a fixed acquisition time of 2 min $step^{-1}$ at room temperature. Sample preparation for XRD analysis involved gentle grinding of the solid into a fine powder and packing of approximately 0.5 g of the sample into the aluminum sample holder.

Room temperature Fourier Transformed Infrared spectroscopy (FTIR) of the samples in KBr pellets (2.0 mg of sample/200 mg of KBr) were recorded using a Bomem MB104 spectrometer in the range 4000–500 cm^{-1} by averaging 32 scans at a maximum resolution of 8 cm^{-1}.

The morphology of the samples was examined by a Phenom ProX (Phenom World B.V., Eindhoven, The Netherlands) scanning electron microscope (SEM) equipped with an energy-dispersive X-ray spectroscopy (EDX) detector (Phenom World B.V.). The acquired data were processed using the ProSuite software integrated with the Phenom Element Identification software, which allowed the quantification of the elements present in the samples both in weight and atomic concentration. The samples were placed into aluminum pin stubs with electrically conductive carbon adhesive tape (PELCO Tabs™), which were subsequently placed inside a Phenom Charge Reduction Sample Holder (CHR); different points were then analyzed for elemental composition with a mapping intensity of 15 kV.

Inductively coupled plasma atomic emission spectroscopy (ICP-AES) analyses were performed with a 5110 ICP-OES spectrometer (Agilent Technologies) to determine the contents of Na, Al, Si (*i.e.* the typical elements in zeolites), and Fe, according to the procedure described in [20].

Surface area and pore volume were determined from the nitrogen adsorption/desorption isotherms at − 196 °C, using a Carlo Erba (Sorptomatic Instruments CE Series) gas adsorption device. Before analysis, all samples were outgassed at 250 °C under vacuum (7.5×10^{-3} Torr) for 12 h in order to clean the surface from any adsorbed impurities. The isotherms were elaborated according to the BET method, applying the procedure suggested by Rouquerol et al. [25] for the proper calculation of BET surface area of microporous materials. The external surface area (S_{ext}) and micropore volume (V_{micro}) were calculated by the *t*-method. The mesopore volume (V_{meso}) was calculated by the difference between the total pore volume at $P/P^0 = 0.99$ (V_{total}) and V_{micro}.

XPS analysis of the samples was performed using a Kratos Axis-Supra

instrument equipped with aluminum Kα monochromatized radiation at 1486.6 eV X-ray source, within ESCApe software. Due to the not conducting nature of the samples, it was necessary to use a co-axial electron neutralizer to minimize surface charging, which performed the neutralization by itself. XPS Photoelectrons were collected from a take-off angle of 90° relative to the sample surface. The measurement was done in a Constant Analyser Energy mode (CAE) with a 15 mA of emission current and 160 eV and 40 eV pass energy for, respectively, survey spectra and high-resolution spectra. Charge referencing was done by setting the lower binding energy C1s photo peak at 285.0 eV C1s hydrocarbon peak.

Microcalorimetry of ammonia adsorption was used to assess the surface acid properties of the samples. A Tian-Calvet heat flow calorimeter (Setaram) equipped with a volumetric vacuum line was used for the microcalorimetric measurements. Prior to the successive introduction of small doses of the probe gas ammonia (NH_3), a desired amount of samples (0.100 g) was pretreated at 80 °C under vacuum (7.5×10^{-3} Torr) overnight. Successive small doses of NH_3 were introduced onto the samples until a final equilibrium pressure of about 1.2 Torr was achieved. The equilibrium pressure after each adsorbed dose was measured by means of a differential pressure gauge (Datametrics) and the thermal effect recorded. The adsorption temperature was maintained at 80 °C in order to limit physisorption. After outgassing overnight at the same temperature, a second run was carried out to determine the amount of the probe gas irreversibly adsorbed by subtracting from the first one (which allowed the assessment of the overall uptake of the probe gas) the second isotherm, obtained after outgassing the sample. The adsorption (amount of adsorbed probe gas *vs.* the corresponding equilibrium pressure) and calorimetric (integral heat of adsorption *vs.* the corresponding equilibrium pressure) isotherms were acquired from each adsorption run. Combining the adsorption and calorimetric data, a plot of the differential heat of adsorption (Q_{diff}, kJ mol^{-1}) as a function of the adsorbed amount (n_A, μmol g^{-1}) was drawn, which gives information on the influence of the surface coverage on the energetics of the adsorption.

2.3. Electrochemistry

Electrochemical measurements were performed using a thermostated three-electrode cell assembly composed of an Hg/Hg_2Cl_2 (sat. KCl) reference electrode, a platinum foil (99.95%) counter electrode and a Toray carbon paper (geometrical area of 4.0 cm^2) working electrode. The reference electrode was separated from the electrolyte solution by a Habber-Luggin capillary tip. The Toray carbon paper was glued to the platinum wire using conductive carbon cement (Quintech) and was dried at room temperature for 24 h. All electrochemical measurements were conducted at the controlled temperature of 25 °C. The electrochemical instrumentation consists of a potentiostat/galvanostat from Amel Instruments coupled to a computer (i5) through an AD/DA converter. The Labview software (National Instruments) and a PCI-MIO-16E-4 I/O module were used for generating and applying the potential program as well as acquiring data such as current intensities. The catalytic ink was ultrasonically prepared by dispersing the iron-zeolite powder sample (20 mg) prepared previously in a mixture of ultra-pure water (Millipore system, 18.2 MΩ cm at 20 °C) and Nafion® suspension (5 wt% Sigma-Aldrich®). An iron-zeolite loading of 5.0 mg cm^{-2} of catalytic ink was homogeneously deposited onto the wet proofed Toray carbon paper and the solvent was then evaporated at room temperature. Prior to electrochemical measurements, the solution is de-aerated with ultra-pure N_2 (U Quality from Air Liquide) for 30 min, and a nitrogen stream is maintained over the solution during the measurements in order to avoid any dissolved oxygen interferences. The anodic catalytic activity of the iron-zeolite modified electrodes was investigated by using cyclic voltammetry (CV) both in the absence and presence of 0.036 mM (25 ppm) of Congo Red (CR, $C_{32}H_{22}N_6Na_2O_6S_2$, 3,3′-([1,1′-biphenyl]−4,4′-diyl)bis(4-aminonaphthalene-1-sulfonic acid $C_{14}H_6Na_2O_7S$, Sigma-Aldrich®, Scheme 1) in NaCl (0.10 mol L^{-1}), at room temperature.

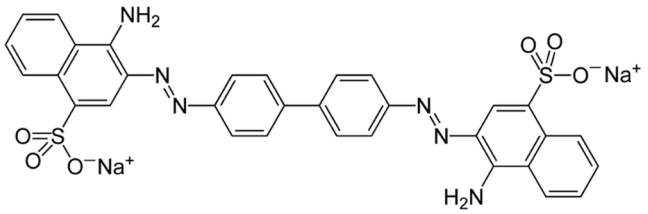

Scheme 1. Molecular structure of Congo Red (CR) dye.

Electro Fenton-like oxidation at a constant potential of 2.0 V *vs.* SCE, in the presence of CR (0.072 mM, 50 ppm), was carried out in a two-compartment cell with an ion exchange membrane (Nafion®−417, membrane thickness 0.017 in.), separating the anode and cathode compartments, at room temperature.

Electrolysis products were analyzed by high performance liquid chromatography (HPLC) equipped with an isocratic pump (Jasco PU-980 Inteligent HPLC Pump), and a double on-line detection including an UV-Vis detector (Jasco Inteligent UV/vis detector) and a RI Detector (Shimadzu). The products partition was carried out in an ion exchange columns, Aminex HPX-87 H from Biorad (λ = 210 and 260 nm) and a reverse phase RP18 column from Merck (λ = 497 nm) for HPLC. Ion Chromatography (Dionex DX-100) with AS11HC analytical column and guard column was used for the quantification of ionic oxidation products.

For purposes of comparison with the electrochemical studies, the sample Fe(H)ZSM-5 was used as heterogeneous catalyst for the oxidation of CR using catalytic conditions similar to those described in [18, 20]. The reaction was performed at room temperature and 40 °C, without addition of acid, with 12.0 mM of H_2O_2 and the semi-batch reactor was filled with 250 mL of a 50 ppm CR solution and 200 mg L^{-1} of the catalyst, during 240 min.

The total organic carbon (TOC) was determined using the NPOC method in Shimadzu's Total Organic Carbon Analyzer TOC-L, coupled with the ASI-L autosampler of the same brand.

3. Results and discussion

3.1. Physicochemical characterization of Fe(III)-zeolite samples

The different iron-zeolite samples based in MFI and FAU structures were prepared by ion exchange method, which implies that the Fe(III) counter-ions replace the pristine cations in the same location to maintain the electroneutrality of the structure. The Fe(III)-MFI samples were prepared by the different pathways 1, 2 and 3 shown in Fig. 1a. Samples obtained from routes 1 and 2 should be similar since the heat treatment in 2 leads to the elimination of NH_3. However, for the purposes of the work, the sample from path 1 has been named as Fe(H)ZSM-5 and the one from path 2 as $Fe(NH_4)$ZSM-5. Likewise, the sample obtained by direct ion exchange of the sodium ions with Fe(III) using NaY as the pristine zeolite (Fig. 1b) was named Fe (Na)Y_{nano}. In our previous works, we showed that the MFI and FAU zeolite structures have different average particle sizes, herein NaY_{nano} presents nanosized particles of 150 nm in size [26], whereas (NH_4)ZSM-5 reveals irregular particles, with large aggregates, medium and small particles (2500, 760 and >100 nm, respectively) [27].

XRD diffraction patterns of representative samples ((NH_4)ZSM-5, Fe(H)ZSM-5, Fe(Na)ZSM-5, NaY_{nano} and Fe(Na)Y_{nano}) are shown in Fig. 2a.

All Fe-exchanged zeolite samples show the same peak positions of the typical XRD patterns of highly crystalline MFI or FAU zeolites, similar to those reported in the literature for these structures, without evidence of the presence of new metal phases [3,28]. For the FAU-based samples, the peaks located at 15.7, 18.7, 20.4, 23.4, 26.9, 30.6, 31.2, and 33.8° correspond, respectively, to the reflection planes (331), (333), (440), (533), (642), (555), (822) and (644) of the highly crystalline

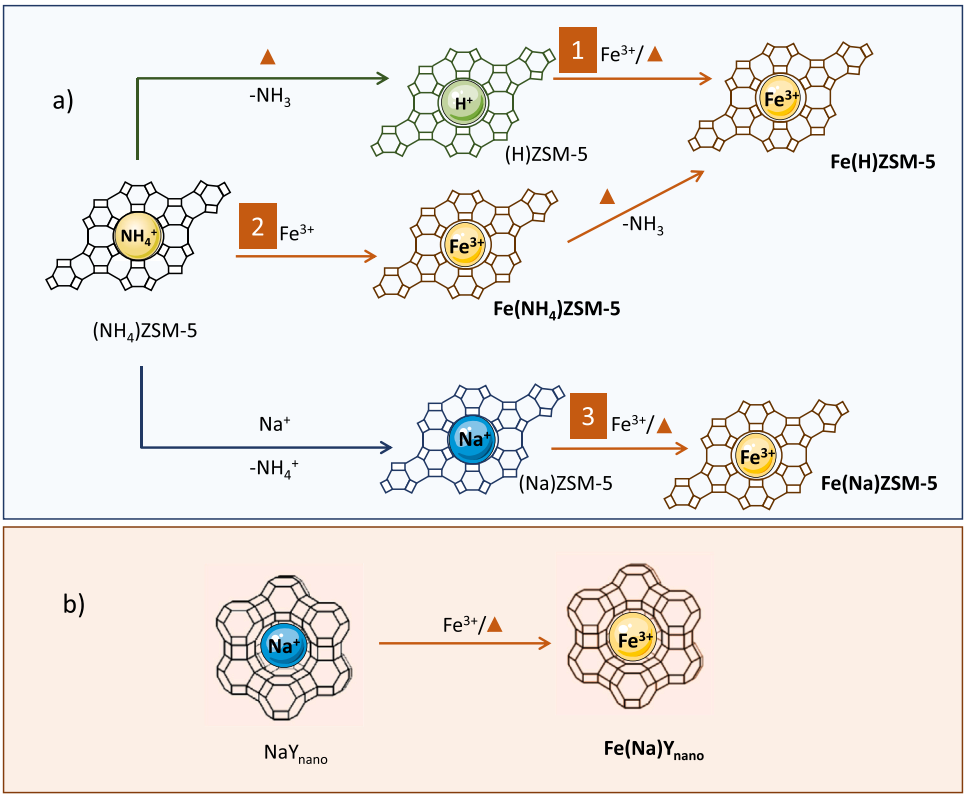

Fig. 1. Schematic representation of the different routes for preparing the Fe(III)-exchanged zeolite samples: a) MFI and b) FAU zeolite structures.

Y zeolite structure, which is in good agreement with the results reported in the literature [28,29]. However, the introduction of iron species in NaY_{nano} reveals a decrease in the peaks intensity, suggesting that the crystallinity of the structure was affected by the ion-exchange method used.

Similarly, the X-ray diffraction patterns of the (NH_4)ZSM-5, Fe(H)ZSM-5 and Fe(Na)ZSM-5 samples exhibit the typical pattern of ZSM-5 crystallographic structure from MFI family. The five characteristic diffraction peaks at about 7.8, 8.7, 22.9, 23.7 and 24.3° correspond to (101), (020), (501), (303), and (133) reflection planes of ZSM-5 [28,30], respectively. It is noted that the XRD patterns of the prepared Fe-containing remain almost unchanged after the exchange with Fe(III) ions, with a small decrease in the relative intensity of the peaks compared to the pristine zeolites, suggesting that replacing of the original cations by iron ions have similar preferences in their locations in zeolite structure [3,20,31].

This conclusion is further confirmed by FTIR analysis presented in Fig. 2b and Fig. S1, which shows that the characteristic zeolite bands remain unchanged after the exchange with the Fe(III) ions, as confirmed in [26,32,33]. Fig. 2b in the spectral region of 2000–500 cm^{-1} shows the fundamental lattice vibrations for the zeolite structures [32,33] considering surface hydroxyl groups of Si-OH stretching (as evidenced by the broad band at 3700–2800 cm^{-1} reported in Fig. S1). Moreover, the absorption bands at about 1053 and 982 cm^{-1} (MFI and FAU structures, respectively) are attributed to the internal asymmetric stretching of Si-O-X, whereas the band centered around 784 cm^{-1} is due to the external symmetric stretching vibration of the X-O (X = Si or Al) bond [32–37]. Likewise, the absorption bands at around 1209, 624 and 534 cm^{-1} correspond to those characteristic of the five member rings of the *pentasil* type MFI zeolite structure (ZSM-5) [35,37]. The band at 1628 cm^{-1} is ascribable to the typical H-O-H bending vibration mode, resulting from water adsorbed on the zeolite structure, whose amount becomes smaller for the ZSM-5 based zeolites, due to the high total Si/Al ratio of this structure (SiAl = 14.90), as also confirmed by the decreased intensity of the band at around 3458 cm^{-1} (Fig. S1). These results are consistent with our previous studies on zeolites exchanged with copper, nickel or silver ions [35,36]. The studies of Hammond et al. showed that the absence of a band at 710–700 cm^{-1} suggests a migration of the Fe ions from the framework to extra-framework positions, which could boost the catalytic activity of the Fe(III)-MFI samples [38].

The N_2 adsorption/desorption isotherms acquired at − 196 °C are reported in Fig. S2. According to the IUPAC classification, Types I plus IV isotherms were identified for the pristine zeolites, with prevalence of Type I, due to the mainly microporous character, even if in the presence of a not negligible mesoporosity highlighted by the presence of hysteresis loops, especially in the case of NaY_{nano} as a consequence of the nanospaces in the aggregates of the zeolite particles [26]. Regardless of the ion exchange procedure used (Fig. 1), the Fe-samples retained the same shape of the original isotherms. The resulting textural properties are shown in Table 1.

All Fe(III)-exchanged zeolite samples possess high surface areas (in the range 360–394 $m^2\ g^{-1}$ and equal to 853 $m^2\ g^{-1}$ for MFI- and FAU-supported samples, respectively) as well as high mesopore surface areas (in the range 140–161 $m^2\ g^{-1}$ and equal to 137 $m^2\ g^{-1}$ for MFI- and FAU-supported samples, respectively), which are inferior to those of the starting zeolites whatever the preparation procedure. However, the good textural properties preserved after the introduction of the Fe(III) ions suggest that such ions are homogeneously incorporated, probably in the same locations as the original cations.

In general, in the heterogeneous catalysts the metal ions introduced are stabilized by structure and connected to other atoms that provide more reactivity of catalysts [39,40]. The zeolite structure with high surface area and arranged porous arrays, boosts the better spatial dispersion of the metal ions and promotes a fast mass transfer process, which enhances the reactivity of these catalysts through a high accessibility of the active sites by reactants from the external medium [19,40].

SEM micrographs in Fig. 3(a-d) reveal the presence of particles

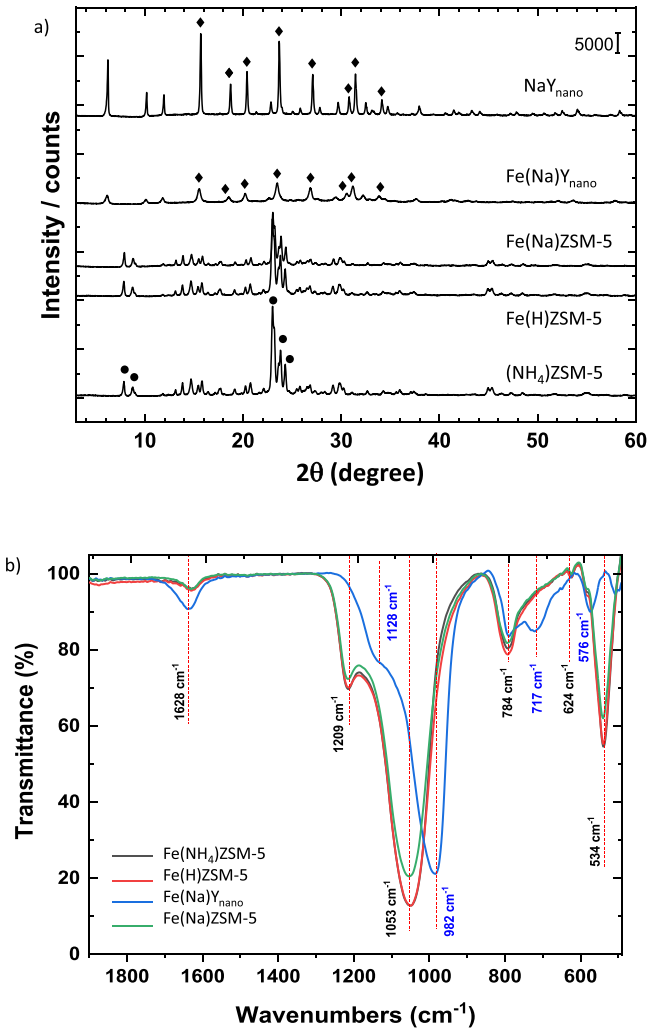

Fig. 2. a) XRD diffraction patterns of: (NH$_4$)ZSM-5, Fe(H)ZSM-5, Fe(Na)ZSM-5, Fe(Na)Y$_{nano}$ and NaY$_{nano}$; b) FTIR spectrum of Fe(NH$_4$)ZSM-5, Fe(H)ZSM-5, Fe(Na)ZSM-5 and Fe(Na)Y$_{nano}$ in the spectral region of 2000–500 cm^{-1}.

Table 1
Physicochemical properties of the pristine zeolites and Fe-exchanged zeolite samples.

Samples	S^a_{BET} ($m^2\ g^{-1}$)	V^b_{total} ($cm^3\ g^{-1}$)	S^c_{ext} ($m^2\ g^{-1}$)^b	V^c_{micro} ($cm^3\ g^{-1}$)	V^d_{meso} ($cm^3\ g^{-1}$)
(NH$_4$)ZSM-5	401	0.26	185	0.09	0.17
Fe(NH$_4$)ZSM-5	384	0.27	153	0.09	0.18
HZSM-5	455	0.28	200	0.11	0.17
Fe(H)ZSM-5	397	0.28	161	0.10	0.18
NaZSM-5	379	0.27	158	0.09	0.18
Fe(Na)ZSM-5	360	0.26	140	0.09	0.17
NaY$_{nano}$	833	0.51	172	0.25	0.26
Fe(Na)Y$_{nano}$	853	0.36	137	0.26	0.10

[a]Surface area calculated from the BET equation; [b]Total pore volume determined from the amount adsorbed at $P/P_o = 0.99$; [c]External surface area and micropore volume calculated by the *t*-method; [d]Mesopore volume calculated by the difference V_{total}-V_{micro}

typical for MFI, with clumped morphology and slightly different sizes (approximately 100 nm), which indicate that the typical morphology of the pristine zeolite was preserved after the exchange with Fe(III). The same results were obtained for the FAU sample, whose images are shown in Fig. S3. As expected, EDX analysis of Fe(Na)ZSM-5 (Fig. 3f), as well as, of NaY$_{nano}$ and Fe(Na)Y$_{nano}$ (Fig. S3) shows the presence of the following elements: O, Si, Al, Na, and Fe, confirming that the method used for the introduction of the iron species is suitable, not drastic, and leads to stable Fe-catalysts, in agreement with XRD, FTIR and N_2-physisorption data.

The chemical composition of the samples was determined by ICP-AES. For the pristine zeolites, only the presence of Si, Al and Na was confirmed, no other metal impurities being detected (Table S1). The calculated total Si/Al ratio was 14.90 and 1.88 for (NH$_4$)ZSM-5 and NaY$_{nano}$, respectively. As for the Fe-containing catalysts, different amounts of Fe ions should be exchanged due to the different ion exchange capacity of the MFI and FAU zeolite structures. As expected, the iron content is higher for the NaY$_{nano}$-based sample (Table 2) due to the higher aluminum content of the structure, which allows a better ion exchange capacity.

As expected, the amount of iron is higher for the NaY$_{nano}$-based sample due to the higher aluminum content of the structure which allows a better ion exchange capacity. In the case of the samples prepared from ZSM-5, the amount of iron follows the order Fe(NH$_4$)ZSM-5 < Fe(H)ZSM-5 < Fe(Na)ZSM-5. This outcome is related to the diffusion capacity of the counter-ion, which is better for H^+ and Na^+ than for NH_4^+ during the ion exchange with the ferric ions (Figure1).

The presence of ferric ions in the samples Fe(NH$_4$)ZSM-5 and Fe(Na)Y$_{nano}$ was confirmed by XPS analysis, which can make available valuable information regarding the oxidation state of the elements at the surface by analyzing the binding energy (BE) regions of Si 2p, Al 2p, O 1 s, C 1 s, and Fe 2p. For Fe(NH$_4$)ZSM-5 and Fe(Na)Y$_{nano}$, peak deconvolution was performed on the high-resolution spectra of the Fe 2p region (Fig. 4). Distinct peaks in the Fe $2p_{1/2}$ and Fe $2p_{3/2}$ binding energies regions are detected for Fe(Na)Y$_{nano}$ in the range 725–729 eV and 710–719 eV, respectively, which appear broadened and have a rather poor signal-to-noise ratio, due to the low amount of iron.

Similar results were observed by Bandala et al. [41] for Fe-containing samples based on BEA zeolites. These authors showed that the Fe 2p core lines are distinguished into well-separated spin–orbit doublet structures (Fe $2p_{3/2}$ and $2p_{1/2}$), with respective shake-up strong satellites that overlap the main photoelectron lines. They also reported that the value of BE and of the doublet splitting are strongly dependent on the iron ionic states. In our case, the values of Fe $2p_{3/2}$ binding energies are higher than 710 eV, which, according to the NIST XPS database and other published works, correspond to ferric ions [41–45] in the state of counter-ions of the negative framework. Bandala et al. suggested that such ions are located into zeolite framework in tetrahedral surroundings [41]. In the case of Fe(NH$_4$)ZSM-5, for which the iron loading is remarkably lower than for Fe(Na)Y$_{nano}$, the peaks in the Fe 2p BE region were not observable. From the XPS results, the amount of Fe(III) at the surface was also quantified (Table 2). It was found that the iron amount quantified by XPS for Fe(NH$_4$)ZSM-5 is similar to the bulk iron content, suggesting a homogeneous distribution of ferric ions throughout the MFI structure. Probably, a fraction of Fe(III) ions is located in extra-framework positions and could enhance the catalytic activity of these samples, as suggested in the literature [38].

Concerning Fe(Na)Y$_{nano}$, due to the different sites where the iron ions can be located in the FAU structure, the lower amount at the surface than in bulk suggests their location within the inner cavities [44].

The surface acid properties of the catalysts were determined by adsorption microcalorimetry of ammonia. The results are reported in Fig. 5 in terms of differential heat of adsorption (Q_{diff}) *vs.* ammonia uptake (n_A), which gives information on the influence of the surface coverage on the adsorbent-adsorbate interaction energy. All curves show a continuously decreasing trend of Q_{diff} *vs.* ammonia coverage, pointing out to the existence of energetically heterogeneous adsorption sites. Very high initial values of Q_{diff} (in the range 270–450 kJ mol^{-1}), which steeply decline to lower values, can be observed, suggesting the presence of a small number of very strong acid sites. At high coverage values, physisorption can take place, and its contribution to the ammonia uptake should be neglected in the assessment of the acid sites

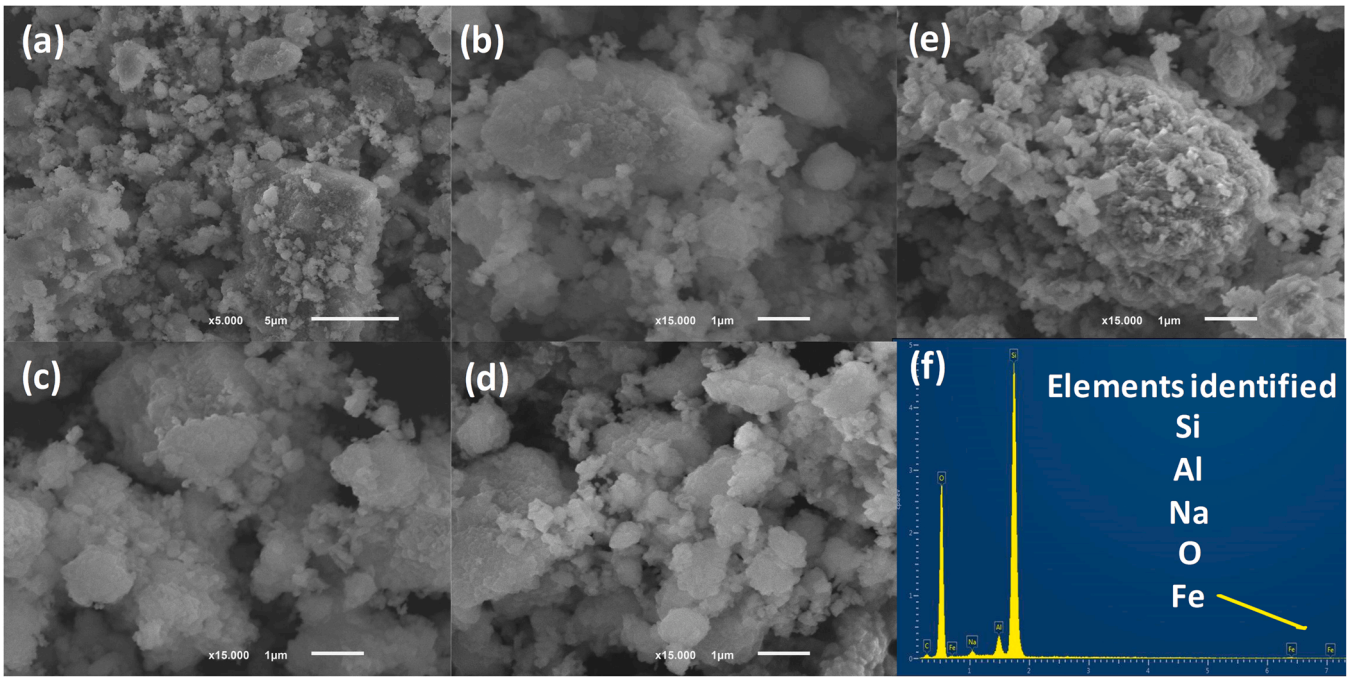

Fig. 3. SEM images of (NH_4)ZSM-5 at different magnification (a,b), Fe(H)ZSM-5 (c), Fe(NH_4)ZSM-5 (d), Fe(Na)ZSM-5 (e), and EDX spectrum of Fe(Na)ZSM-5 (f).

Table 2
Elemental composition of pristine zeolites and Fe(III)-zeolite samples.

Samples	Si/Al[a]	Fe (wt%)[a]	Fe (wt%)[b]
(NH_4)ZSM-5	14.90	–	–
Fe(NH_4)ZSM-5	14.79	0.33	0.36
Fe(Na)ZSM-5	14.68	0.73	nd
Fe(H)ZSM-5	14.77	0.41	nd
NaY_{nano}	1.88	–	–
Fe(Na)Y_{nano}	2.03	1.32	1.04

[a]Quantified by ICP-AES analysis; [b]Quantified by XPS analysis; nd – not determined.

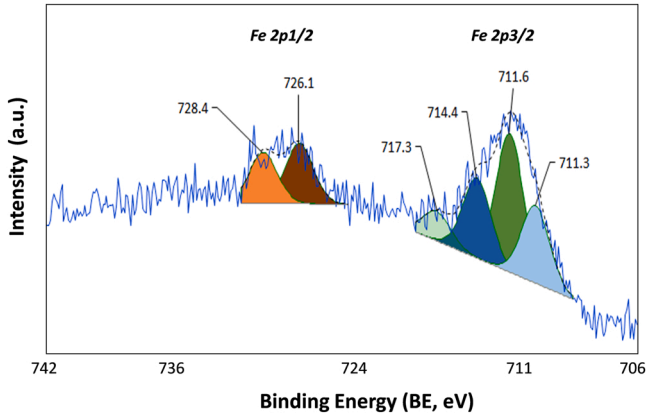

Fig. 4. Peak deconvolution of the high-resolution XPS spectra of the Fe 2p region of Fe(Na)Y_{nano} and Fe(NH_4)ZSM-5.

concentration. By considering that all samples show differential adsorption heats in the range 58–70 kJ mol^{-1} at high coverage, a Q_{diff} value of 70 kJ mol^{-1} has been assumed as the cut-off between specific and non-specific adsorbent/adsorbate interactions. Such value corresponds to about three times the NH_3 condensation heat (20.2 kJ mol^{-1} at 80 °C) [27,45], and thus to the heat which is typically considered to be released during physisorption (*i.e.*, two or three times as large as the condensation heat of the probe molecule [45]. In view of the above, the fraction of ammonia coverage corresponding to differential heats below 70 kJ mol^{-1} has been neglected in the assessment of the concentration of acid sites, which have been roughly ranked as weak ($n_{A,weak}$, $70 \leq Q_{diff} \leq 90$ kJ mol^{-1}), medium ($n_{A,medium}$, $90 < Q_{diff} \leq 150$ kJ mol^{-1}), and strong ($n_{A,strong}$, $Q_{diff} > 150$ kJ mol^{-1}). The threshold value of 90 kJ mol^{-1} to distinguish between sites of weak and medium strength has been chosen by taking into account the lowest Q_{diff} value corresponding to the irreversible adsorption of ammonia. The microcalorimetric results are summarized in Table S2.

As for the pristine MFI zeolite, the total NH_3 uptake ($n_{A,tot}$) is in the order NaZSM-5 < HZSM-5 < NH_4ZSM-5. By calculating the sites strength distribution in terms of percentage (Fig. 6), it results that, as expected, NaZSM-5 shows the highest percentage of weak acid sites (72%), which falls below 50% for both NH_4ZSM-5 and HZSM-5, mostly in favor of medium strength sites that, in the case of HZSM-5, account for 60% of the total ones. Interestingly, except for HZSM-5, which possesses a higher acidity compared to Fe(H)ZSM-5, the presence of ferric ions leads to an increase in acidity, as can be noted by the higher percentage of both medium and strong sites for Fe(Na)ZSM-5 and Fe(NH_4)ZSM-5 in comparison with the corresponding pristine zeolites. Regarding the Fe (III)-zeolite samples, surface acidity is in the order Fe(NH_4)ZSM-5 > Fe(H)ZSM-5 > Fe(Na)ZSM-5.

Noteworthy, in the case of NaY_{nano}, the curve of Fe(Na)Y_{nano} stays above that of the pristine zeolite in the range of medium-strength acid sites, clearly indicating that Fe addition makes the surface more acidic, as already observed for the other Fe-containing ZSM-5 samples. In particular, the acid properties of Fe(Na)Y_{nano} are comparable to those of (Na)ZSM-5 and Fe(Na)ZSM-5. In terms of percentage, NaY_{nano} presents 73% of weak sites, 15% of medium-strength ones, and 12% of strong sites, whereas the Fe-containing sample shows 65%, 29% and 6% of weak, medium-strength, and strong acid sites, respectively, which is comparable with NaZSM-5.

After the introduction of iron, the more acidic surface was obtained for the samples based in MFI structure, in terms of fraction of both strong and medium-strength sites. The samples Fe(NH_4)ZSM-5 and Fe(H)ZSM-5 show a comparable number of acid sites (Table S2), which confirms

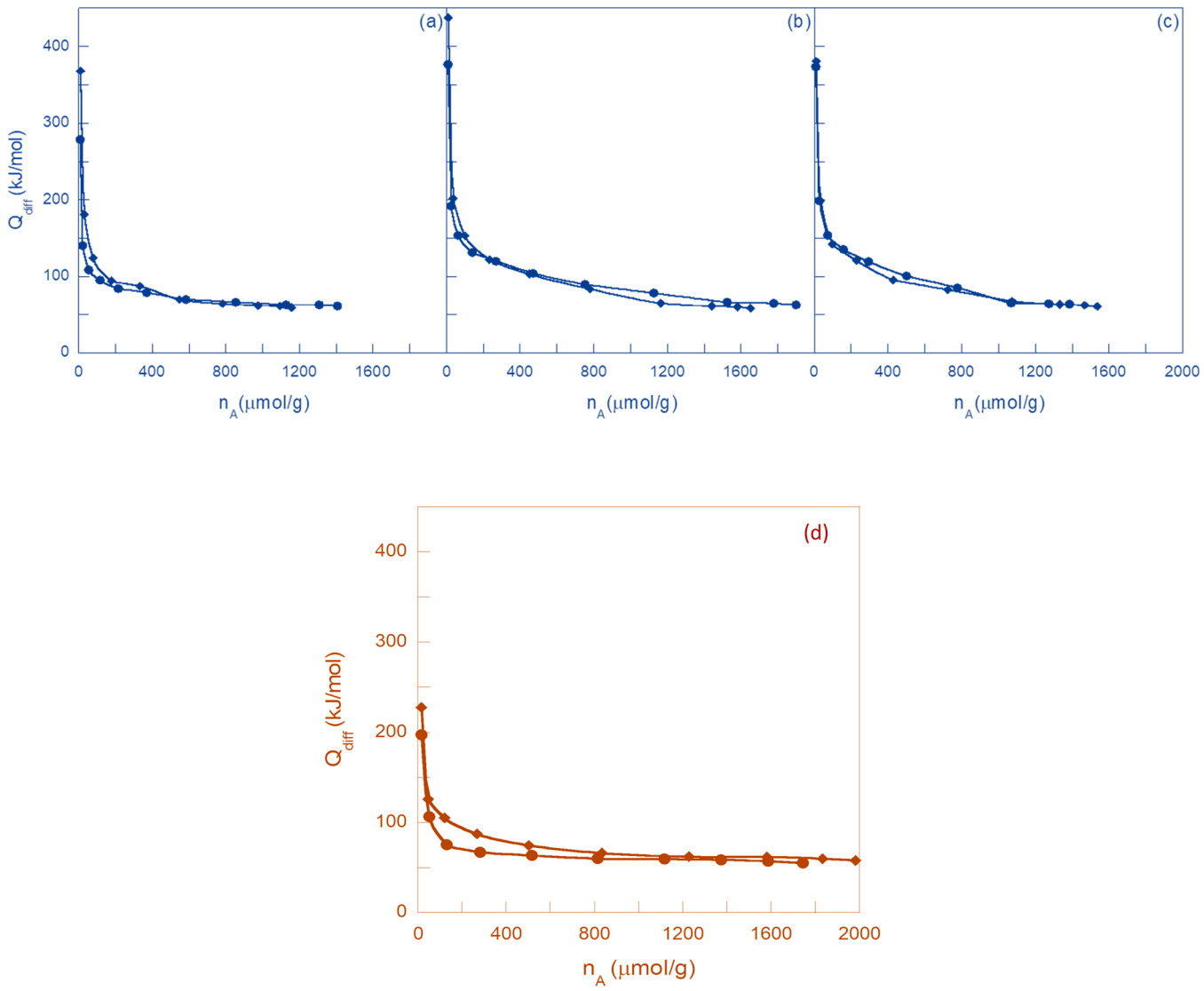

Fig. 5. Differential heat of adsorption as a function of NH_3 coverage for the pristine (•) and Fe-exchanged (◆) ZSM-5 zeolites: a) NaZSM-5 and Fe(Na)ZSM-5; b) NH_4ZSM-5 and Fe(NH_4)ZSM-5; c) HZSM-5 and Fe(H)ZSM-5; d) NaY_{nano} (•) and Fe(Na)Y_{nano} (◆).

that the calcination step allows the decomposition of the ammonium ions and the subsequent elimination of ammonia (NH_3) leading to the protonic form (Fig. 1). Based on their acidic properties, it was expected that both the catalysts have the same behaviour in electro Fenton-like oxidation.

3.2. *Electrochemical degradation of congo red dye on modified iron-zeolite samples*

The presence of hydrogen peroxide (H_2O_2) is mandatory for the heterogeneous catalysis by Fenton reaction using solids supports [14,18,20]. So, Fe(H)ZSM-5 was tested as heterogeneous catalyst using the same concentration of CR as that used in electrolysis, 0.072 mM (50 ppm). At room temperature and 12 mM H_2O_2, the degradation was not observed, whereas at the temperature of 40 °C and the same concentration of H_2O_2, the degradation achieved 75% of conversion after 240 min, with 31% of mineralization. It is important to point out that, the pH of the Fenton reaction was controlled by the zeolite itself, since the MFI structure has strong acidic properties (Fig. 6).

The use of H_2O_2 and higher applied temperatures can be avoided by employing more sustainable methods like electrochemical ones. In this context, the electrochemical studies were carried out with different Fe (III)-zeolite samples without the addition of hydrogen peroxide, at room temperature, for CR degradation. Blank tests were carried out using the pristine zeolites (ZSM-5 and NaY_{nano}) in the presence of dye (50 ppm), under the experimental conditions for Fenton-like catalysis and electrocatalysis, at room temperature, both in the absence and in the presence of H_2O_2. It was observed that the dye degradation does not occur in the blank tests and that the presence of iron species enhances the catalytic activity of the modified Fe(III)-zeolite electrodes at room temperature without H_2O_2.

3.2.1. *Modified Fe(III)-MFI zeolite electrodes*

The electrochemical behavior of Congo Red dye, a typical azo dye (Scheme 1) on modified Fe(III)-exchanged zeolite electrodes, Fe(Na)ZSM-5 and Fe(H)ZSM-5 was studied by cyclic voltammetry (CV) in the presence of 25 ppm of CR, in 0.1 mol L^{-1} NaCl, at room temperature. Fig. 7 presents the cyclic voltammograms of the modified Fe(Na)ZSM-5 electrode as an example, recorded at a scan rate of 50 mVs^{-1}.

In absence of CR, two redox processes, an irreversible and a quasi-reversible one, can be noticed in 0.10 mol L^{-1} NaCl medium, the first one corresponding to − 1.3/− 0.65 V *vs.* SCE, is probably related to Fe (0)/Fe(II) species while, the second (0.3/0.5 V *vs.* SCE) can be attributed to Fe(II)/Fe(III) couple. The oxidation of CR starts at 0.8 V *vs.* SCE, after

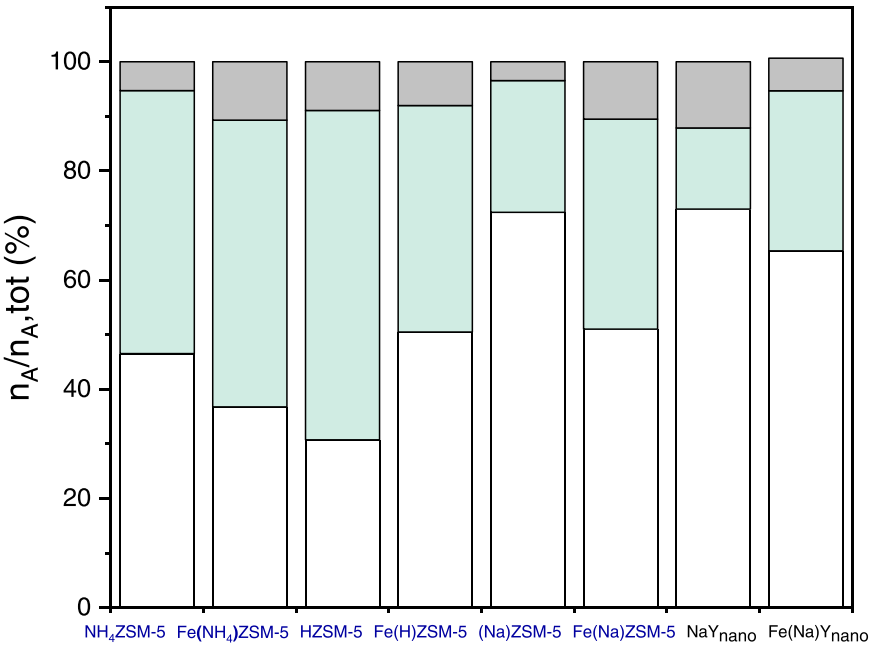

Fig. 6. Percentage of acid sites of different strength for the pristine zeolites and the corresponding Fe-exchanged samples: (□), weak sites; (▭), medium sites; (▭) and strong sites.

the oxidation of Fe(II) into Fe(III), indicating that the presence of Fe(III) species on the electrode surface is necessary for the oxidation of this organic dye. Similar redox processes were observed for the other Fe(H)ZSM-5 and Fe(NH_4)ZSM-5 modified electrodes. The presence of these redox couples was confirmed by CV obtained in Fe(III) nitrate medium, which confirms the presence of these species (Fig. S4). Iron species mediated oxidation can be foreseen as given in Scheme 2, as reported in [14]:

During the reverse scan of the CV analysis, a reduction peak can be noticed at − 0.7 V *vs.* SCE, due to the reduction of previously oxidized species. Voltammetry study also provides evidence concerning the rate-determining step of the CR oxidation process. The slope of the log(I/mA) *vs.* v(mVs^{-1}) curves in 0.10 mol L^{-1} NaCl medium corresponds to 0.60 to Fe(Na)ZSM-5, 0.74 to Fe(H)ZSM-5 and 0.72 to Fe(NH_4)ZSM-5. These results show that the for Fe(Na)ZSM-5 kinetic of the electrochemical reaction was governed by the diffusion step while for the other modified electrodes both diffusion and adsorption steps have influence on reaction rate [14,46–48].

The electrolysis of 0.072 mM (50 ppm) CR with the Fe(Na)ZSM-5 and Fe(H)ZSM-5 modified zeolite electrodes, was carried out with an applied potential of 2 V *vs.* SCE, at room temperature. The voltammograms at the beginning and at the end of the electrolysis for both the electrodes are displayed in Fig. 8. The increase in the overall current intensities noticed at the end of the electrolysis, can be attributed to the restructuration of the electrode surface, including an increase of the active surface, due to the oxidative treatment during the electrolysis. The contribution of the current intensities resulting from the oxidation of some electrolysis products must be also foreseen.

During the electrolysis, a gradual discoloration of the electrolytic solution was observed, indicating the degradation of the pristine dye at

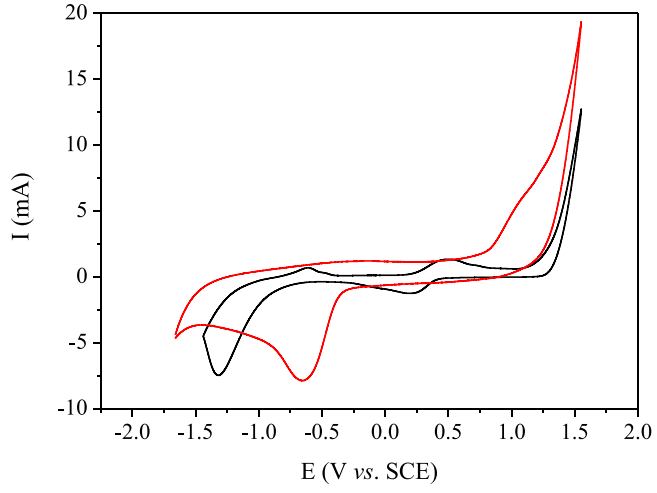

Fig. 7. Cyclic voltammograms of Fe(Na)ZSM-5 modified zeolite electrode recorded at 50 mVs^{-1} in the absence of dye (black curve) and in the presence of 0.036 mM of Congo Red dye (red curve) in NaCl (0.10 mol L^{-1}).

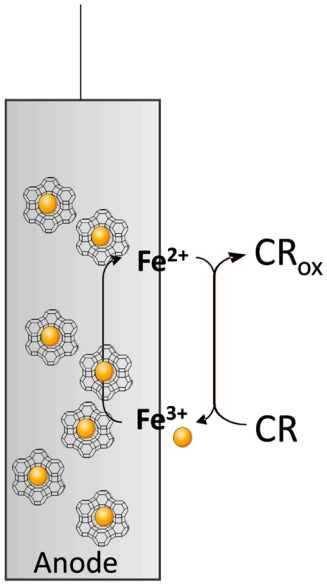

Scheme 2. Schematic of the catalytic reaction of Fe(II)/Fe(III) and CR [14].

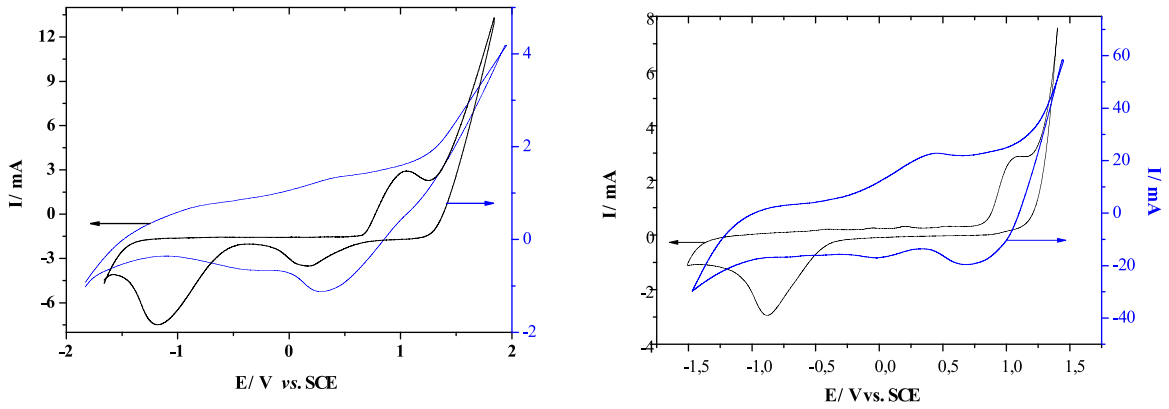

Fig. 8. Cyclic voltammograms of modified zeolite electrodes, Fe(Na)ZSM-5 and Fe(H)ZSM-5 respectively, recorded at 50 mVs^{-1} at the beginning (blue line) and at the end of the electrolysis (black line) of 0.072 mM of Congo Red dye in NaCl (0.10 mol L^{-1}).

both modified Fe(III)-ZSM-5 electrodes. Remarkably, the lower amounts of iron quantified in MFI samples (Table 2) are enough to trigger the reaction. UV/vis spectra of the solutions collected, at the beginning, during, and at the end of the electrolysis, are presented in Fig. 9. At the end of the electrolysis an important decrease of absorbance was noticed, in the visible region at 480 nm, which corresponds to the wavelength of maximum absorbance for CR, due to its highly conjugated structure. This result confirms the significant degradation of the initial substrate due to the fragmentation of the azo bonds by oxidation, with the consequent discoloration of the solution in the anode compartment observed during electrolysis. In addition, the observed decrease in the intensity of the two bands in the UV region at respectively 350 and 490 nm, are attributed to the degradation and opening of the aromatic ring of the CR dye [49–51]. A control experiment in the absence of the modified electrode showed that the degradation of the dye does not occur under the same conditions.

Quantification of the products at the end of the electrolysis was carried out by HPLC-UV and IC (ionic chromatographic) analyses. At the end of the electrolysis, carboxylic acids coming from the opening of the CR rings were identified as formic, oxalic, tartaric, glutaric, and oxamic acids. The total amount of carboxylic acids corresponding to 28% and 16% of the oxidized CR were detected for Fe(Na)ZSM5 and Fe(H)ZSM5 modified electrodes, respectively. In addition, different concentrations of the sulfate ion were found, in Fenton-like reaction, for these modified

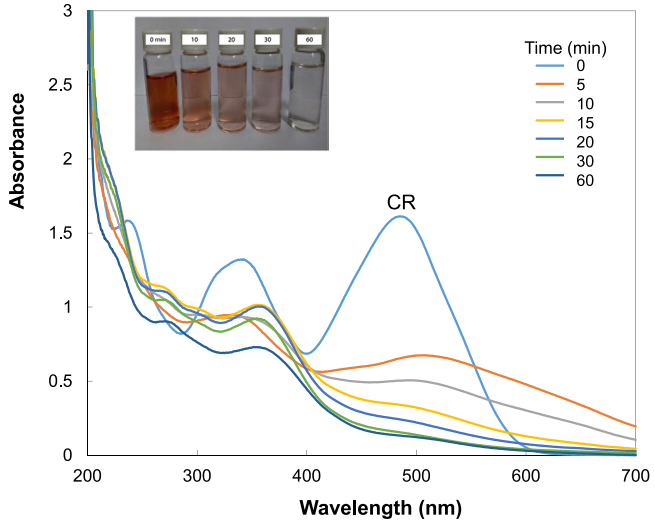

Fig. 9. UV/vis spectra of the 0.072 mM of CR dye solution at the beginning (blue line) at different electrolysis time and at the end of the electrolysis in Fe(Na)ZSM-5 modified zeolite electrode (60 min) in 0.10 mol L^{-1} NaCl medium.

zeolite electrodes. At the end of electrolysis, the concentration of the SO_4^{2-} ions, detected by IC, reached 0.03 mM and 0.05 mM, for Fe(Na) ZSM5 and Fe(H)ZSM5 modified electrodes, respectively. The distribution of the products seems to be related to the acidic properties of the Fe (III)-MFI samples (Fig. 6). The evolution of the concentration of CR and of the sulfate ions during the electrolysis is presented in Fig. 10.

It could be confirmed from these results that the low molecular weight carboxylic acids that are refractory compounds, do not undergo a further oxidation leading to mineralization. The extent of the mineralization was determined by TOC analysis at the end of the electrolysis (60 min) for the three Fe(III)-MFI modified electrodes, with a mineralization degree of 64%, 40%, and 26%, for Fe(H)ZSM-5, $Fe(NH_4)$ZSM-5 and Fe(Na)ZSM-5 modified electrodes, respectively. The higher mineralization observed for the first two electrodes are related to the distribution of the acid sites in the modifying zeolites, for the reason that of their preparation (Fig. 1). Remarkably, the amount of iron affects the mineralization rate, with samples with lower Fe contents favoring higher mineralization degrees comparing with Fe(Na)ZSM-5 (Table 2).

The kinetic curves of the reaction for CR and sulfate ions (Fig. 10) show that a very important degradation rate was obtained in the first 10 min of reaction. After 10 min, 74% of CR was degraded at all the Fe (III)-MFI modified electrodes. The complete conversion of dye into oxidation products was achieved after 45 min, while the mineralization was determined at the end of the electrolysis.

Within the first 20 min, a linear trend is observed for ln C *vs.* t (s), which proves that the reaction is first order with respect to CR for all MFI-modified electrodes. The slope of the straight line gives a rate constant (k) equal to 3.0×10^{-3} s^{-1}, for both Fe(Na)ZSM-5 and Fe(H)ZSM-5, and 1.0×10^{-3} s^{-1} for $Fe(NH_4)$ZSM-5. The lower value of k corresponding to the latter indicates that the reaction kinetics are slower in this case, which can be related to the preparation of this material (Fig. 1). These results are in agreements with those obtained from scan rate study which shows that the reaction kinetics were governed in a different way for the first electrode and for the last two electrodes. It can be also concluded that while Fe(Na)ZSM-5 modified electrode provides higher oxidation for pristine compound, the further oxidation of intermediate compounds are not favored since the mineralization rate is lower in this case. This result can be explained by the higher need of $OH^{\bullet}$ radicals for the oxidation of recalcitrant compounds like low molecular weight carboxylic acid, depending on the acidic properties of the electrode material.

3.2.2. *Modified Fe(III)-FAU zeolite electrode*

The cyclic voltammograms of the $Fe(Na)Y_{nano}$-modified electrode, in 0.1 M NaCl medium, with and without CR dye at room temperature, are displayed in Fig. 11. The anodic and cathodic peaks observed at 0.30 and 0.50 V *vs.* SCE, respectively, can be attributed to the redox process of the Fe(II)/Fe(III) couple. The current intensities of these peaks are lower

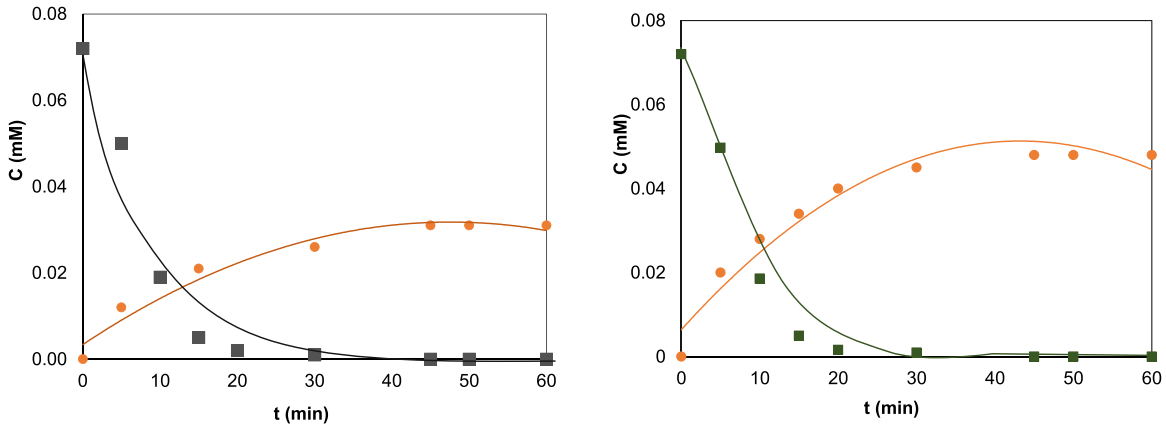

Fig. 10. Concentration of CR (■) and SO_4^{2-} ion (•) *vs.* electrolysis time for the electrooxidation of 0.072 mM CR at Fe(Na)ZSM-5 and Fe(H)ZSM-5 modified electrodes, respectively.

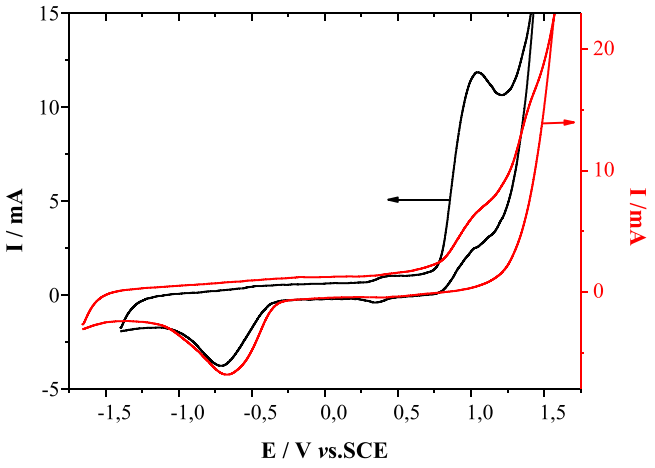

Fig. 11. Cyclic voltammograms of the Fe(Na)Y_{nano} modified electrode recorded at 50 mVs^{-1} in the absence of dye (black curve) and in the presence of 0.036 mM of Congo Red dye (red curve) in NaCl (0.10 mol L^{-1}).

than those found for the Fe-MFI-modified electrodes. This result could be related to the lower amount of acid sites on this zeolite, despite the higher content of exchanged iron ions (Table 2 and Fig. 6). Contrary to what observed for the modified electrodes with the Fe-MFI zeolites, no significant current intensities were noticed in the presence of the CR dye. The decrease in current intensities in 0.70 and 1.10 V *vs.* SCE comparing with the previous cases was accompanied by a shift of oxygen evolution potential. This shift can be related to the adsorption of the organic compounds on the electrode surface, occupying the active sites necessary for the oxidation of the solvent.

The electrolysis of 0.072 mM (50 ppm) of CR dye on the Fe(Na)Y_{nano}-modified electrode at 2.0 V *vs.* SCE at room temperature, provides the total degradation of the pristine compound after 2 h. Remarkably, in the case of the FAU structure, electrolysis takes twice as long to achieve full dye degradation, which is probably due to the distribution of the iron species, preferably located within the inner cavities, even though the amount of iron is higher than Fe(III)-MFI samples, as displayed in Table 2. The reaction is first order with respect to CR with Fe(Na)Y_{nano} the rate constant being 1.2×10^{-3} s^{-1}.

The total amount of oxidation products (*i.e.*, formic, oxalic, and glutaric acids) detected at the end of the electrolysis does not exceed 20% of the initial CR, while TOC analysis shows a mineralization extent of 19%, lower than that found for the Fe-MFI samples. These results show that, for the electrode modified with Fe(Na)Y_{nano} zeolite, the conversion of the CR dye into oxidation products occurs easily, while their mineralization is not easy to achieve. Considering the potential influence of surface properties, especially pH of the electrode material the oxidation of CR was carried out on more acidic zeolite structure.

As mentioned in our previous work, the formation of Fe(III)-hydroperoxo species can be foreseen in this case, considering the presence of oxygen produced at 2 V *vs.* SCE from the oxidation of water in the adopted oxidative conditions and the acidic reaction medium provided by the zeolite itself [14]. Since the silanol groups of the zeolite structures are able to stabilize the different active iron species, a Fenton-like reaction can be suggested with further steps for the production of the reactive oxygenated radical species starting from Fe (III)-hydroperoxo as described in Eqs. (3) and (4).

$$[Fe(III)OOH]zeo + O_2 + H^+ \leftrightarrows [Fe(II)OH]zeo + HOO^{\bullet} \quad (3)$$

$$[Fe(III)OOH]zeo \leftrightarrows [Fe(IV)O]zeo + HO^{\bullet} \quad (4)$$

At the final stage, the important decrease of absorbance observed with the vanishing of the sharp bands at 350 and 490 nm (Fig. 9) show that the main chromophores in the dye molecule were degraded by the electro-generation of the oxygenated radical species that promote low molecular organic acids and sulfate ions, followed by mineralization (Fig. 12).

The oxidation of CR molecules at the Fe(III)-zeolite-modified electrodes produce several intermediates, like aromatic by-products that decompose to carboxylic acids, which in turn undergo total mineralization. The higher mineralization rate obtained for Fe-exchanged MFI structures most probably depends on their acidic properties, bringing the acidic pH of the Fenton-like reaction due to the presence of isolated catalytic sites, since the pristine zeolite has lower aluminum content.

As mentioned before, few works are reported in literature using modified zeolite electrodes on electro Fenton-like oxidation in order to degrade dye pollutants [11–14,52–54]. For example, in the presence of Fe-ZSM-5 (Fe loading = 10 wt%), Acid blue 25 dye (200 ppm) was degraded 90% in 2 h (pH = 3, I = 500 mA and catalyst concentration of 100 ppm) [53]. In the other relevant studies on electro Fenton-like oxidation, different times of dye degradation were found: Reactive red 120 azo (10 ppm, ≈ 98% in 30 min, pH = 3, I = 0.10 A and 0.5 g L^{-1} of catalyst) [12]; Reactive black 5 (100 ppm, ≈ 100% in 1.5 h, pH = 2, I = 0.6 V and 0.5 g L^{-1} of catalyst) [54]; Acid Orange 7 (35 ppm, ≈ 100% in 40 min, pH = 6.4 and 0.1 g L^{-1} of catalyst) [13]. However, when we compare ours Fe(III)-zeolite-modified electrodes prepared in this work, the most important feature is that the total degradation of Congo Red dye occurs in 1 h for MFI zeolite and 2 h for FAU zeolite with high mineralization rates, without H_2O_2 and the zeolites themselves control the pH of the medium reaction.

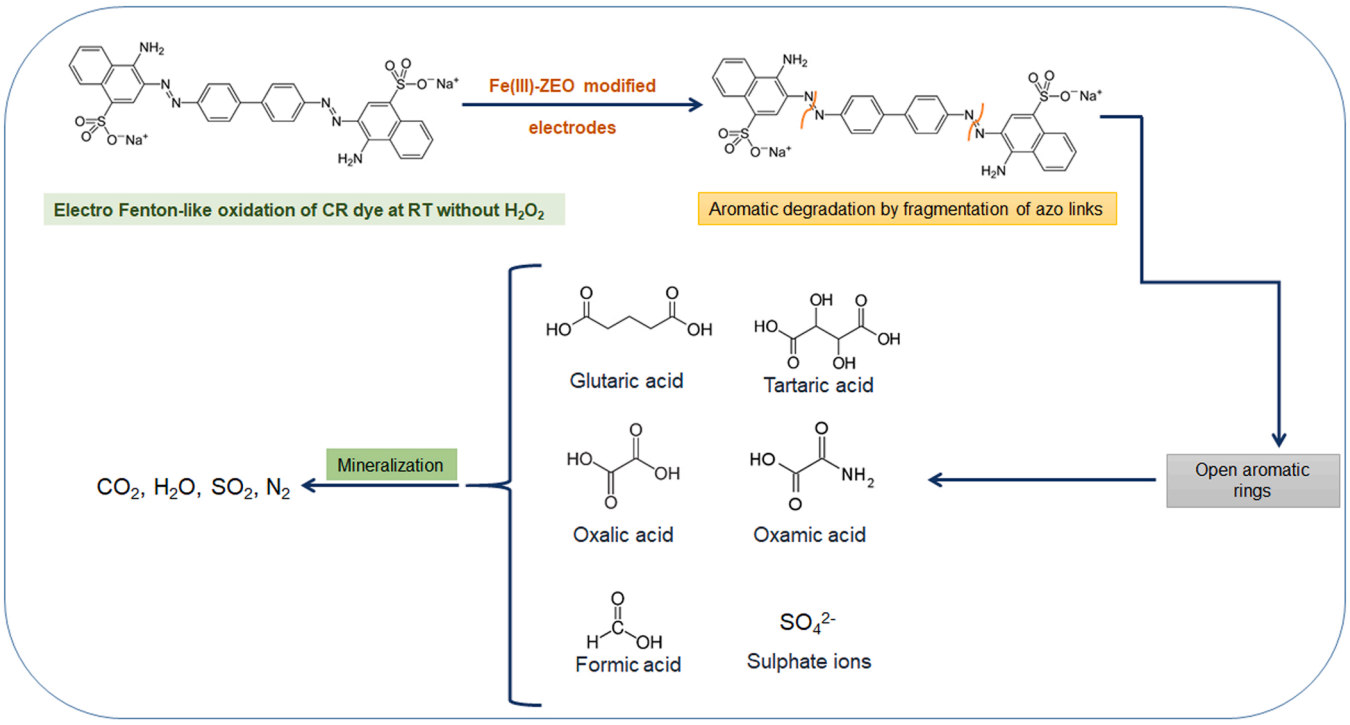

Fig. 12. Proposed electro Fenton-like degradation pathway of CR using Fe(III)-zeolite-modified electrodes.

4. Conclusion

The electrocatalytic degradative oxidation of CR with high mineralization rate was achieved in this study with different Fe(III)-zeolite samples prepared starting from two different structures, MFI and FAU. The results show the effect of the Fe(III)-zeolite-modified electrodes in Fenton-like oxidation, with special focus on the oxidation of the intermediate refractory compounds. The highest mineralization yield was obtained for the electrode modified with Fe(H)ZSM-5, with a satisfactory rate constant, 1×10^{-3} s^{-1}, which corresponding to a fast degradation of the pristine dye. The different mineralization rates observed for the Fe(III)-exchanged MFI and FAU zeolite structures have been ascribed to their surface acidic properties, as well as to the different iron amount quantified in the samples. In fact, the acidic properties of the zeolite are determinant for better degradation and the modified electrodes prepared with MFI structure allows the best results. This study highlighted that the electrochemical method allows faster mineralization of CR, avoiding the use of redox agents at room temperature. For a sustainable process, these results look promising to be applied in water treatments.

CRediT authorship contribution statement

Zineb Bencheqroun: Formal analysis, Investigation, Writing – original draft. **Nihat E. Sahin:** Investigation, Writing – original draft, Visualization. **Olívia S.G.P. Soares:** Investigation, Writing – review & editing. **Manuel F.R. Pereira:** Investigation, Writing – review & editing. **Hicham Zaitan:** Validation, Supervision. **Mustapha Nawdali:** Validation. **Elisabetta Rombi:** Investigation, Validation, Writing – review & editing, Supervision. **António M. Fonseca:** Methodology, Writing – review & editing, Supervision, Funding acquisition. **Pier Parpot:** Methodology, Validation, Writing – review & editing, Supervision, Funding acquisition. **Isabel C. Neves:** Conceptualization, Methodology, Validation, Writing – review & editing, Supervision, Funding acquisition. All authors have read and agreed to the published version of the manuscript.

Declaration of Competing Interest

There are no conflicts of interest to declare.

Acknowledgments

Z.B. thanks to ERASMUS+ Program for the mobility PhD grant. This research work has been funded by national funds funded through FCT/MCTES (PIDDAC), (Fundação para Ciência e Tecnologia, FCT) over the projects: LA/P/0045/2020 (ALiCE), UIDB/50020/2020 and UIDP/50020/2020 (LSRE-LCM), Centre of Chemistry (UID/QUI/0686/2020) and project BioTecNorte (operation NORTE-01-0145-FEDER-000004), supported by the Northern Portugal Regional Operational Programme (NORTE 2020), under the Portugal 2020 Partnership Agreement, through the European Regional Development Fund (ERDF).

Appendix A. Supporting information

Supplementary data associated with this article can be found in the online version at doi:10.1016/j.jece.2022.107891.

References

[1] Ch Gao, F. Lyu, Y. Yin, Encapsulated metal nanoparticles for catalysis, Chem. Rev. 121 (2) (2021) 834–881, https://doi.org/10.1021/acs.chemrev.0c00237.
[2] S. Shwan, M. Skoglundh, L.F. Lundegaard, R.R. Tiruvalam, T.V.W. Janssens, A. Carlsson, P.N.R. Vennestrøm, Solid-state ion-exchange of copper into zeolites facilitated by ammonia at low temperature, ACS Catal. 5 (1) (2015) 16–19, https://doi.org/10.1021/cs5015139.
[3] O.S.G.P. Soares, L. Marques, C.M.A.S. Freitas, A.M. Fonseca, P. Parpot, J.J. M. Órfão, M.F.R. Pereira, I.C. Neves, Mono and bimetallic NaY catalysts with high performance in nitrate reduction in water, Chem. Eng. J. 281 (2015) 411–417, https://doi.org/10.1016/j.cej.2015.06.093.
[4] H. Dong, L. Zhang, Z. Fang, W. Fu, T. Tang, Y. Feng, T. Tang, Acidic hierarchical zeolite ZSM-5 supported Ru catalyst with high activity and selectivity in the seleno-functionalization of alkenes, RSC Adv. 7 (36) (2017) 22008–22016, https://doi.org/10.1039/C7RA01732D.
[5] M. Álvaro, J.F. Cabeza, D. Fabuel, H. García, E. Guijarro, J.L. Martínez de Juan, Electrical conductivity of zeolite films: influence of charge balancing cations and crystal, Struct. Chem. Mater. 18 (1) (2006) 26–33, https://doi.org/10.1021/cm050467e.

[6] N. Densakulprasert, L. Wannatong, D. Chotpattananont, P. Hiamtup, A. Sirivat, J. Schwank, Electrical conductivity of polyaniline/zeolite composites and synergetic interaction with CO, Mater. Sci. Eng. B 117 (3) (2005) 276–282, https://doi.org/10.1016/j.mseb.2004.12.006.

[7] S. Wang, Y. Peng, Natural zeolites as effective adsorbents in water and wastewater treatment, Chem. Eng. J. 156 (2010) 11–24, https://doi.org/10.1016/j.cej.2009.10.029.

[8] M. Oliveira, A. Araújo, G. Azevedo, M.F.R. Pereira, I.C. Neves, A.V. Machado, Kinetic and equilibrium studies of phosphorous adsorption: Effect of physical and chemical properties of adsorption agent, Ecol. Eng. 82 (2015) 527–530, https://doi.org/10.1016/j.ecoleng.2015.05.020.

[9] H. Serati-Nouri, A. Jafari, L. Roshangar, M. Dadashpour, Y. Pilehvar-Soltanahmadi, N. Zarghami, Biomedical applications of zeolite-based materials: a review, Mater. Sci. Eng. C 116 (2020), 111225, https://doi.org/10.1016/j.msec.2020.111225.

[10] N. Vilaça, A.R. Bertão, E.A. Prasetyanto, S. Granja, M. Costa, R. Fernandes, F. Figueiredo, A.M. Fonseca, L. De Cola, F. Baltazar, I.C. Neves, Surface functionalization of zeolite-based drug delivery systems enhances their antitumoral activity in vivo, Mater. Sci. Eng. C. 120 (2021), 111721, https://doi.org/10.1016/j.msec.2020.111721.

[11] V. Poza-Nogueiras, E. Rosales, M. Pazos, M.Á. Sanromán, Current advances and trends in electro-Fenton process using heterogeneous catalysts – a review, Chemosphere 201 (2018) 399–416, https://doi.org/10.1016/j.chemosphere.2018.03.002.

[12] M. Rostamizadeh, A. Jafarizad, S. Gharibian, High efficient decolorization of reactive red 120 azo dye over reusable Fe-ZSM-5 nanocatalyst in electro-Fenton reaction, Sep. Purif. Technol. 192 (2018) 340–347, https://doi.org/10.1016/j.seppur.2017.10.041.

[13] T.X.H. Le, M. Drobek, M. Bechelany, J. Motuzas, A. Julbe, M. Cretin, Application of Fe-MFI zeolite catalyst in heterogeneous electro-Fenton process for water pollutants abatement, Microporous Mesoporous Mater. 278 (2019) 64–69, https://doi.org/10.1016/j.micromeso.2018.11.021.

[14] M. Ferreira, N.E. Sahin, A.M. Fonseca, P. Parpot, I.C. Neves, Oxidation of pollutants via an electro-Fenton-like process in aqueous media using iron–zeolite modified electrodes, New J. Chem. 45 (2021) 12750–12757, https://doi.org/10.1039/d1nj01077h.

[15] E. Brillas, C.A. Martínez-Huitle, Decontamination of wastewaters containing synthetic organic dyes by electrochemical methods. An updated review, Appl. Catal. B 166–167 (2015) 603–643, https://doi.org/10.1016/j.apcatb.2014.11.016.

[16] P.V. Nidheesh, M. Zhou, M.A. Oturan, An overview on the removal of synthetic dyes from water by electrochemical advanced oxidation processes, Chemosphere 197 (2018) 210–227, https://doi.org/10.1016/j.chemosphere.2017.12.195.

[17] J.L. Wang, L.J. Xu, Advanced oxidation processes for wastewater treatment: formation of hydroxyl radical and application, Crit. Rev. Environ. Sci. 42 (3) (2012) 251–325, https://doi.org/10.1080/10643389.2010.507698.

[18] M.L. Rache, A.R. García, H.R. Zea, A.M.T. Silva, L.M. Madeira, J.H. Ramírez, Azo-dye orange II degradation by the heterogeneous Fenton-like process using a zeolite Y-Fe catalyst—Kinetics with a model based on the Fermi's equation, Appl. Catal. B 146 (2014) 192–200, https://doi.org/10.1016/j.apcatb.2013.04.028.

[19] Z. Tang, P. Zhao, H. Wang, Y. Liu, W. Bu, Biomedicine meets Fenton chemistry, Chem. Rev. 121 (4) (2021) 1981–2019, https://doi.org/10.1021/acs.chemrev.0c00977.

[20] B.L.C. Santos, P. Parpot, O.S.G.P. Soares, M.F.R. Pereira, E. Rombi, A.M. Fonseca, I. C. Neves, Fenton-type bimetallic catalysts for degradation of dyes in aqueous solutions, Catalysts 11 (2021) 32, https://doi.org/10.3390/catal11010032.

[21] A. Fabiańska, A. Białk-Bielińska, P. Stepnowski, S. Stolte, E.M. Siedlecka, Electrochemical degradation of sulfonamides at BDD electrode: Kinetics, reaction pathway and eco-toxicity evaluation, J. Hazard. Mater. 280 (2014) 579–587, https://doi.org/10.1016/j.jhazmat.2014.08.050.

[22] N.P. Shetti, S.J. Malode, R.S. Malladi, S.L. Nargund, S.S. Shukla, T.M. Aminabhavi, Electrochemical detection and degradation of textile dye Congo red at graphene oxide modified electrode, Microchem. J. 146 (2019) 387–392, https://doi.org/10.1016/j.microc.2019.01.033.

[23] M. Zhang, Q. Shi, X. Song, H. Wang, Z. Bian, Recent electrochemical methods in electrochemical degradation of halogenated organics: a review, Environ. Sci. Poll. Res. 26 (11) (2019) 10457–10486, https://doi.org/10.1007/s11356-019-04533-3.

[24] N. Vilaça, A.F. Machado, F. Morais-Santos, R. Amorim, A.P. Neto, E. Logodin, M.F. R. Pereira, M. Sardo, J. Rocha, P. Parpot, A.M. Fonseca, F. Baltazar, I.C. Neves, Comparison of different silica microporous structures as drug delivery systems for in vitro models of solid tumors, RSC Adv. 7 (2017) 13104–13111, https://doi.org/10.1039/c7ra01028a.

[25] J. Rouquerol, P. Llewellyn, F. Rouquerol, Is the BET Equation Applicable to Microporous Adsorbents?, In Characterization of Porous Solids VII; Llewellyn, P., Rodriguez-Reinoso, F., Rouquerol, J., Seaton, N., Eds.; Elsevier: Amsterdam, The Netherlands, 2007; Vol. 160, pp. 49–56.

[26] N. Vilaça, R. Amorim, A.F. Machado, P. Parpot, M.F.R. Pereira, M. Sardo, J. Rocha, A.M. Fonseca, I.C. Neves, F. Baltazar, Potentiation of 5-fluorouracil encapsulated in zeolites as drug delivery systems for in vitro models of colorectal carcinoma, Coll. Surf. B Biointerfaces 112 (2013) 237–244, https://doi.org/10.1016/j.colsurfb.2013.07.042.

[27] P. Peixoto, J.F. Guedes, E. Rombi, A.M. Fonseca, C. Almeida-Aguiar, I.C. Neves, Metal ion-zeolite materials against resistant bacteria, MRSA, Ind. Eng. Chem. Res. 60 (2021) 12883–12892, https://doi.org/10.1021/acs.iecr.1c01736.

[28] Collection of Simulated XRD Powder Patterns for Zeolites, M.M.J. Treacy and J.B. Higgins (Eds), Published on behalf of the Structure Commission of the International Zeolite Association, Fourth Revised Edition, Elsevier: Amsterdam, The Netherlands, 2001.

[29] H. Awala, J.-P. Gilson, R. Retoux, P. Boullay, J.-M. Goupil, V. Valtchev, S. Mintova, Template-free nanosized faujasite-type zeolites, Nat. Mater. 14 (4) (2015) 447–451, https://doi.org/10.1038/nmat4173.

[30] K.A. Sashkina, E.V. Parkhomchuk, N.A. Rudina, V.N. Parmon, The role of zeolite Fe-ZSM-5 porous structure for heterogeneous Fenton catalyst activity and stability, Microporous Mesoporous Mater. 189 (2014) 181–188, https://doi.org/10.1016/j.micromeso.2013.11.033.

[31] S. Chen, J. Popovich, W. Zhang, C. Ganser, S.E. Haydel, D.-K. Seo, Superior ion release properties and antibacterial efficacy of nanostructured zeolites ion-exchanged with zinc, copper, and iron, RSC Adv. 8 (2018) 37949–37957, https://doi.org/10.1039/C8RA06556J.

[32] A.M. Fonseca, S. Gonçalves, P. Parpot, I.C. Neves, Host–guest chemistry of the (N, N′-diarylacetamidine)rhodium(iii) complex in zeolite Y, Phys. Chem. Chem. Phys. 11 (29) (2009) 6308–6314, https://doi.org/10.1039/B901762N.

[33] C.M.A.S. Freitas, O.S.G.P. Soares, J.J.M. Órfão, A.M. Fonseca, M.F.R. Pereira, I. C. Neves, Highly efficient reduction of bromate to bromide over mono and bimetallic ZSM5 catalysts, Green Chem. 17 (8) (2015) 4247–4254, https://doi.org/10.1039/C5GC00777A.

[34] M.A. Ali, B. Brisdon, W.J. Thomas, Synthesis, characterization and catalytic activity of ZSM-5 zeolites having variable silicon-to-aluminum ratios, Appl. Catal. A 252 (1) (2003) 149–162, https://doi.org/10.1016/S0926-860X(03)00413-7.

[35] L. Ferreira, C. Almeida-Aguiar, P. Parpot, A.M. Fonseca, I.C. Neves, Preparation and assessment of antimicrobial properties of bimetallic materials based on NaY zeolite, RSC Adv. 5 (47) (2015) 37188–37195, https://doi.org/10.1039/C5RA04960A.

[36] I. K.-Biernacka, K. Biernacki, A.L. Magalhães, A.M. Fonseca, I.C. Neves, Catalytic behavior of 1-(2-pyridylazo)-2-naphthol transition metal complexes encapsulated in Y zeolite, J. Catal. 278 (2011) 102–110, https://doi.org/10.1016/j.jcat.2010.11.022.

[37] A.R. Bertão, N. Pires, A.M. Fonseca, O.S.G.P. Soares, M.F.R. Pereira, T. Dong, I. C. Neves, Modification of microfluidic paper-based devices with dye nanomaterials obtained by encapsulation of compounds in Y and ZSM5 zeolites, Sens. Actuators B 261 (2018) 66–74, https://doi.org/10.1016/j.snb.2018.01.071.

[38] C. Hammond, M.M. Forde, M.H.A. Rahim, A. Thetford, Q. He, R.L. Jenkins, N. Dimitratos, J.A. Lopez-Sanchez, N.F. Dummer, D.M. Murphy, A.F. Carley, S. H. Taylor, D.J. Willock, E.E. Stangland, J. Kang, H. Hagen, C.J. Kiely, G. J. Hutchings, Direct catalytic conversion of methane to methanol in an aqueous medium by using copper-promoted Fe-ZSM-5, Angew. Chem. Int. Ed. 51 (2012) 5129–5133, https://doi.org/10.1002/anie.201108706.

[39] P.Y. Dapsens, C. Mondelli, J. Pérez-Ramírez, Design of Lewis-acid centres in zeolitic matrices for the conversion of renewables, Chem. Soc. Rev. 44 (20) (2015) 7025–7043, https://doi.org/10.1039/C5CS00028A.

[40] Z. Zhang, J. Sun, F. Wang, L. Dai, Efficient oxygen reduction reaction (ORR) catalysts based on single iron atoms dispersed on a hierarchically structured porous carbon framework, Angew. Chem. Int. Ed. 57 (2018) 9038–9043, https://doi.org/10.1002/anie.201804958.

[41] E.R. Bandala, R. Sadek, J. Gurgul, K. Łątka, M. Zimowska, L. Valentin, O. M. Rodriguez-Narvaez, S. Dzwigaj, Assessment of the capability of Fe and Al modified BEA zeolites to promote advanced oxidation processes in aqueous phase, Chem. Eng. J. 409 (2021), 127379, https://doi.org/10.1016/j.cej.2020.127379.

[42] A.V. Naumkin, A. Kraut-Vass, S.W. Gaarenstroom, C.J. Powell, NIST X-ray Photoelectron Spectroscopy Database, NIST Standard Reference Database 20, Version 4.1, Last Update to Data Content: 2012, http://dx.doi.org/10.18434/T4T88K;

[43] Y.I. Kim, W.E. Hatfield, Electrical, magnetic and spectroscopic properties of tetrathiafulvalene charge transfer compounds with iron, ruthenium, rhodium and iridium halides, Inorg. Chim. Acta 188 (1991) 15–24, https://doi.org/10.1016/S0020-1693(00)80911-1.

[44] R.V. Siriwardane, J.A. Poston Jr., E.P. Fisher, M.-Sh. Shen, A.L. Miltz, Decomposition of the sulfates of copper, iron (II), iron (III), nickel and zinc: XPS, SEM, DRIFTS, XRD, and TGA study, Appl. Surf. Sci. 152 (1999) 219–236, https://doi.org/10.1016/S0169-4332(99)00319-0.

[45] Y.M. Lee, S.J. Choi, Y. Kim, K. Seff, Crystal structure of an ethylene sorption complex of fully vacuum-dehydrated fully Ag+-exchanged zeolite X (FAU). Silver atoms have reduced ethylene to give CH22- carbanions at framework oxide vacancies, J. Phys. Chem. B 109 (2005) 20137–20144, https://doi.org/10.1021/jp058185p.

[46] D.M. Ruthven, Principles of Adsorption & Adsorption Processes, Wiley, New York, 1984.

[47] V. Ramamurthy, Controlling photochemical reactions via confinement: zeolites, J. Photochem. Photobiol. C 1 (2) (2000) 145–166, https://doi.org/10.1016/S1389-5567(00)00010-1.

[48] E.S. Brigham, P.T. Snowden, Y.I. Kim, T.E. Mallouk, Electron and energy transfer as probes of interparticle ion-exchange reactions in zeolite Y, J. Phys. Chem. 97 (33) (1993) 8650–8655, https://doi.org/10.1021/j100135a019.

[49] M.A. O'Neill, F.L. Cozens, N.P. Schepp, Photogeneration and migration of electrons and holes in zeolite NaY, J. Phys. Chem. B 105 (51) (2001) 12746–12758, https://doi.org/10.1021/jp015518j.

[50] A.-T. Vu, T.N. Xuan, C.-H. Lee, Preparation of mesoporous Fe_2O_3·SiO_2 composite from rice husk as an efficient heterogeneous Fenton-like catalyst for degradation of organic dyes, J. Water Proc. Eng., 28, 2019, pp.169–180, https://doi.org/10.1016/j.jwpe.2019.01.019.

[51] X. Li, J. Zhang, Y. Jiang, M. Hu, S. Li, Q. Zhai, Highly efficient biodecolorization/degradation of congo red and alizarin yellow R by chloroperoxidase from caldariomyces fumago: catalytic mechanism and degradation pathway, Ind. Eng. Chem. Res. 52 (2013) 13572–13579, https://doi.org/10.1021/ie4007563.

[52] A. Gopinath, L. Pisharody, A. Popat, P.V. Nidheesh, Supported catalysts for heterogeneous electro-Fenton processes: recent trends and future directions, Curr. Opin. Solid State Mater. Sci. 26 (2022), 100981, https://doi.org/10.1016/j.cossms.2022.100981. Received 27 September 2021; Received in revised.

[53] A.A. Zahrani, B. Ayati, Using heterogeneous Fe-ZSM-5 nanocatalyst to improve the electro Fenton process for acid blue 25 removal in a novel reactor with orbiting electrodes, J. Electrochem. Chem. 873 (2020), 114456, https://doi.org/10.1016/j.jelechem.2020.114456.

[54] M.Á. Fernández de Dios, O. Iglesias, M. Pazos, M.Á. Sanromán, Application of electro-fenton technology to remediation of polluted effluents by self-sustaining process, Sci. World J. (2014), https://doi.org/10.1155/2014/801870.